• Original Paper •

Evaluating the Impacts of Cloud Microphysical and Overlap Parameters on Simulated Clouds in Global Climate Models※

Haibo WANG[1,3], Hua ZHANG[*2], Bing XIE[4], Xianwen JING[5], Jingyi HE[2], and Yi LIU[1,3]

[1]*Key Laboratory of Middle Atmosphere and Global Environment Observation*, *Institute of Atmospheric Physics*,
Chinese Academy of Sciences, *Beijing* 100029, *China*

[2]*State Key Laboratory of Severe Weather*, *Chinese Academy of Meteorological Sciences*, *Beijing* 100081, *China*

[3]*University of Chinese Academy of Sciences*, *Beijing* 100049, *China*

[4]*Laboratory for Climate Studies*, *National Climate Center*,*China Meteorological Administration*, *Beijing* 100081, *China*

[5]*Department of Climate and Space Sciences and Engineering*, *University of Michigan*, *Ann Arbor* 48109, *USA*

ABSTRACT

The improvement of the accuracy of simulated cloud-related variables, such as the cloud fraction, in global climate models (GCMs) is still a challenging problem in climate modeling. In this study, the influence of cloud microphysics schemes (one-moment versus two-moment schemes) and cloud overlap methods (observation-based versus a fixed vertical decorrelation length) on the simulated cloud fraction was assessed in the BCC_AGCM2.0_CUACE/Aero. Compared with the fixed decorrelation length method, the observation-based approach produced a significantly improved cloud fraction both globally and for four representative regions. The utilization of a two-moment cloud microphysics scheme, on the other hand, notably improved the simulated cloud fraction compared with the one-moment scheme; specifically, the relative bias in the global mean total cloud fraction decreased by 42.9%–84.8%. Furthermore, the total cloud fraction bias decreased by 6.6% in the boreal winter (DJF) and 1.64% in the boreal summer (JJA). Cloud radiative forcing globally and in the four regions improved by 0.3%−1.2% and 0.2%−2.0%, respectively. Thus, our results showed that the interaction between clouds and climate through microphysical and radiation processes is a key contributor to simulation uncertainty.

Key words: cloud fraction, cloud microphysics scheme, cloud radiative forcing, vertical cloud overlap

Article Highlights:

- The utilization of a two-moment cloud microphysics scheme notably improved the simulated cloud-related variables.
- The observation-based approach produced a significantly improved cloud fraction both globally and for four representative regions.
- In the two-moment cloud microphysics scheme, observation-based vertical decorrelation length improved the simulations more obviously than in fixed vertical decorrelation length.

―――――――――――――

1. Introduction

Clouds substantially affect the energy balance of the earth–atmosphere system by reflecting incoming solar radia-tion and absorbing and emitting longwave radiation. Any changes in the macro- and micro-properties of clouds have remarkable effects on the energy balance (Garrett and Zhao, 2006; Intergovernmental Panel on Climate Change, 2013; Fan et al., 2018; Ma et al., 2018). On the other hand, atmospheric dynamic, thermal, and microphysical processes influence the formation and evolution of clouds and their global distribution (Ding et al., 2005). A climate model is a vital tool for understanding the mechanism of climate evolution and predicting climate change. However, much uncertainty

remains in model simulations. Clouds are one of the most crucial sources of such uncertainty (Potter and Cess, 2004). To improve simulation accuracy, cloud distribution and its radiative effects should be represented properly in models (Webb et al., 2001).

The number concentration and effective radius of cloud droplets are key factors that affect the simulations of cloud optical depth, cloud radiation, aerosol-cloud interaction process and so on (Collins et al., 2004). In the past, most global climate models (GCMs) have employed one-moment bulk microphysics schemes (Rasch and Kristjánsson, 1998), in which the model predicts the liquid water content with the prescribed cloud droplet number concentration (CDNC) to diagnose the cloud droplet effective radius (CDER) [see Wang et al. (2014) for the detail]. This simple treatment cannot accurately describe cloud microphysical properties, and more importantly, aerosol-cloud interactions. Morrison and Gettelman (2008) proposed a two-moment cloud microphysics scheme that uses the mass and number concentrations of cloud droplets and ice crystals as predictors in GCMs (Ghan et al., 1997, 2012; Nenes and Seinfeld, 2003; Lohmann et al., 2007; Morrison and Gettelman, 2008). The scheme is suitable for most GCMs and enables a more realistic simulation of cloud microphysical properties. Wang et al. (2014) applied the above two-moment cloud microphysics scheme to the aerosol–climate model BCC_AGCM2.0_CUACE/ Aero (Zhang et al., 2017), thus significantly improving the representation of the aerosol effect on cloud properties.

Additionally, the uncertainty in the description of the vertical overlapping structure of clouds is another obstacle to the accurate representation of the impacts of clouds on climate (Barker et al., 1999). Because the grid sizes of GCMs are often larger than the area covered by clouds at a specific model level, overlap assumptions are essential for describing the overlapping properties of clouds at different vertical levels on the grid (Tompkins and Di Giuseppe, 2015; Wang et al., 2018). Hogan and Illingworth (2000), Mace and Benson-Troth (2002), and Bergman and Rasch (2002) proposed an ingenious approach to describe cloud overlap via the observer-based decorrelation length L_{cf}, which was referred to as general overlap (GenO). Since then, many researchers have applied various methods to obtain L_{cf} (Di Giuseppe, 2005; Kato et al., 2010; Shonk et al., 2010; Oreopoulos et al., 2012; Zhang et al., 2013; Di Giuseppe and Tompkins, 2015; Li et al., 2018, 2019). In general, the simplest way to express the vertical decorrelation length is to set a fixed value globally. Barker (2008) suggested a global value of L_{cf} = 2 km, based on CloudSat and CALIPSO datasets (Stephens et al., 2008). Using the same data, Zhang et al. (2013) calculated seasonal variation in L_{cf} in different regions of East Asia. Di Giuseppe and Tompkins (2015) analyzed the impact of wind shear on L_{cf} based on combined satellite and European Centre for Medium-Range Weather Forecasts reanalysis data. Jing et al. (2018) explored the relationship between L_{cf} and the strength of atmospheric convection in the tropics using a global cloud-resolving model.

The representation of both cloud microphysics and the vertical overlap of fractional clouds influences the simulation of cloud fractions in GCMs, through modifications to microphysical processes and cloud geometry, respectively. Nevertheless, to date, few studies have considered the combination of these two factors. In this work, we applied two cloud microphysical parameterization schemes and different cloud overlap methods using the aerosol–climate model BCC_AGCM2.0_CUACE/Aero, to assess the accuracy of the simulated cloud fraction and other relevant parameters.

The rest of this paper is organized as follows. Section 2 provides a brief introduction to the data, model, and methods; we then analyzed the impact of the two factors on cloud simulations in section 3. The reasons for the resulting effects are discussed in section 4, and the conclusion of the main results is provided in section 5.

2.   Model, data, and methods

2.1.   *Model*

The model used in this study was BCC_AGCM2.0_CUACE/Aero (Zhang et al., 2012). Our radiative transfer model (BCC_RAD) (Randles et al., 2013; Zhang, 2016) was applied in the above model to make radiation calculations. A correlated k-distribution method developed by Zhang et al. (2003) was adopted to treat gas absorptions, of which the 10–49 000 cm^{-1} (0.204–1000 μm) spectral range is divided into 17 bands (8 longwave and 9 shortwave) (Zhang et al., 2006a, b). Five major greenhouse gases (GHGs) – H_2O, CO_2, O_3, N_2O, and CH_4 – as well as chlorofluorocarbons (CFCs) are considered in the longwave region, and H_2O (including continuum absorption), O_3, and O_2 continuum absorptions are considered in the shortwave region [see Zhang (2015) for details]. The optical properties of water and ice clouds have been given by Lu et al. (2011) and Zhang et al. (2015). For a description of the sub-grid cloud structure, such as the vertical overlap of fractional clouds and horizontal inhomogeneity of cloud condensate, the Monte Carlo Independent Column Approximation (McICA) approach was applied to treat cloud overlapping (Pincus et al., 2003; Zhang et al., 2014). The McICA approach is a sub-grid random cloud generator (Räisänen et al., 2004; Räisänen and Barker, 2004) that creates unresolved cloud distributions based on the grid mean cloud profile and auxiliary assumptions about the vertical and horizontal alignment of clouds. A detailed evaluation of the combination of BCC_RAD and McICA to calculate cloud radiation is given by Zhang et al. (2014). The two-moment cloud microphysics scheme was used in the BCC_AGCM2.0_CUACE/Aero model (Morrison and Gettelman, 2008). This model simulates the properties of clouds and radiation balance at the top of the atmosphere more accurately when compared with observations (Wang et al., 2014). A more detailed introduction on radiation calculations, cloud radiation process treatment and the model framework can be found in Zhang (2016) and Zhang et al. (2019).

2.2.   *Data*

The simulated clouds and Earth's radiation budget

(ERB) were evaluated against the satellite-based datasets of the Cloud and Earth's Radiation Energy System (CERES). Here we used total cloud fraction data from the CERES SYN1deg-Month Edition 4.1 product (Minnis et al., 2011), which is based on MODerate resolution Imaging Spectroradiometer (MODIS) retrievals, and radiation flux data from the CERES Energy Balanced and Filled-Month Edition 4.1 product (Loeb et al., 2018), which is based on measurements from CERES instruments hosted on several satellites, along with data from other instruments. The overall uncertainty in $1° \times 1°$ latitude-longitude regional monthly all-sky TOA flux is estimated to be 3 W m^{-2} [one standard deviation (1σ)] for the Terra-only period and 2.5 W m^{-2} for the Terra–Aqua period both for SW and LW fluxes. The SW clear-sky regional monthly flux uncertainty is estimated to be 6 W m^{-2} for the Terra-only period and 5 W m^{-2} for the Terra–Aqua period. The LW clear-sky regional monthly flux uncertainty is 5 W m^{-2} for Terra only and 4.5 W m^{-2} for Terra–Aqua. The data used here are monthly mean fields over the 2006–15 period for both products, with a horizontal resolution of $1° \times 1°$ (https://ceres.larc.nasa.gov/order_data.php).

2.3. Methods

2.3.1. Vertical decorrelation length

Unlike the maximum-random overlap assumed by most large-scale models, GenO avoids the dependence on the vertical resolution of the model. GenO relates the degree of cloud overlap to the vertical distance, thus determining the degree of cloud overlap according to the vertical height difference between two layers of clouds. This method reflects the cloud-type-dependent diversity of cloud overlapping structures (Zhang and Jing, 2016). In GenO, for two layers of clouds at heights of Z_k and Z_l with cloud fractions of C_k and C_l, respectively, the total cloud fraction (C_{tot}) is defined as (Jing et al., 2018)

$$C_{k,l} = \alpha_{k,l} C_{k,l}^{max} + (1 - \alpha_{k,l}) C_{k,l}^{ran}, \qquad (1)$$

where $C_{k,l}^{max} = \max(C_k, C_l)$ and $C_{k,l}^{ran} = C_k + C_l - C_k C_l$ are the total cloud fractions calculated using the maximum overlap and random overlap assumptions, respectively. Then, $\alpha_{k,l}$ represents the overlap coefficient of two-layer clouds. The greater the value of $\alpha_{k,l}$, the higher the overlap of the two-layer clouds. The term $\alpha_{k,l}$ is calculated using the following formula (Bergman and Rasch, 2002):

$$\alpha_{k,l} = \exp\left[-\int_{Z_k}^{Z_l} \frac{dz}{L_{cf}(z)}\right], \qquad (2)$$

where L_{cf} represents the overlapping cloud parameters. Its physical meaning is the distance between the two layers of clouds (Z_k and Z_l) when the overlap coefficient $\alpha_{k,l}$ decays to e^{-1}. Z_k and Z_l represent the respective heights of the middle point of each cloud layer. It can be seen from Eq. (2) that for a given Z_k and Z_l, $\alpha_{k,l}$ increases with L_{cf}. For $C_{k,l}$, a larger L_{cf} corresponds to a smaller $C_{k,l}$, and a smaller L_{cf} corre-

sponds to a larger $C_{k,l}$. L_{cf} is related to cloud and atmospheric dynamics (Naud et al., 2008). $C_{k,l}$ can be described by a sub-grid random cloud generator (Räisänen et al., 2004; Räisänen and Barker, 2004) that creates unresolved cloud distributions based on the grid mean cloud profile and auxiliary assumptions about the vertical and horizontal alignment of clouds. The McICA approach is applied in the model. A detailed evaluation of the combination of random cloud generator and McICA to calculate cloud radiation is given by Zhang et al. (2014).

2.3.2. Cloud radiative forcing

Cloud radiative forcing (CRF) is defined as the difference in net radiation flux between a given atmosphere and the same atmosphere with no clouds (Harrison et al., 1990; Xie et al., 2013; Zhao and Garrett, 2015). The top-of-atmosphere (TOA) shortwave (SW), longwave (LW), and all-band (NET) CRF are expressed as, respectively,

$$SWCRF = FSNT - FSNTC, \qquad (3)$$

$$LWCRF = FLNT - FLNTC, \qquad (4)$$

$$NETCRF = SWCRF + LWCRF, \qquad (5)$$

where FSNT (FLNT) and FSNTC (FLNTC) are the all-sky and clear-sky net TOA SW (LW) radiation flux, respectively.

The radiation ratio, N, is defined as follows (Lu et al., 2004):

$$N = -SWCRF/LWCRF. \qquad (6)$$

If SWCRF cooling dominates, both NETCRF < 0 and $N > 1$, indicating that CRF cools the atmosphere, whereas if LWCRF heating dominates, NETCRF > 0 and $N < 1$, indicating that CRF heats the atmosphere. Moreover, if NETCRF ≈ 0 and $N \approx 1$, the heating effect of LWCRF nearly offsets the cooling effect of SWCRF.

2.3.3. Experiments

The following two vertical decorrelation length treatments were used to describe the treatment of cloud overlap in the BCC_AGCM2.0_CUACE/Aero model: (1) a global mean value of $L_{cf} = 2$ km was applied everywhere, and (2) temporally and spatially varying L_{cf} (hereinafter, referred to as L_{cf}^*) values calculated from the CloudSat/CALIPSO satellite datasets for each model grid and each calendar month following the method by Jing et al. (2016).

Table 1 summarizes the experimental design of this study. Four experiments were conducted with different combinations of the two L_{cf} schemes and the two cloud microphysics schemes. In each experiment, the model was run for 35 years, with the results of the most recent 30 years used in the analysis. Experiments 3 and 4 (EXP3/4), both with one-moment cloud microphysics but different overlap treatments, were similar to those carried out by (Wang et al., 2018), emphasizing coverage globally and over East Asia.

Table 1. Experimental design.

Experiments	Model	Parameter	Time (yr)
EXP1	two-moment	L_{cf}=2 km	35
EXP2	two-moment	L_{cf}^*	35
EXP3	one-moment	L_{cf}=2 km	35
EXP4	one-moment	L_{cf}^*	35

Experiments 1 and 2 (EXP1/2) were similar to EXP3/4 in terms of the overlap treatment but were extended to the two-moment microphysics scheme. This allowed for further evaluation with respect to the effects of cloud microphysics on cloud fraction simulations in GCMs.

3.   Results

3.1. L_{cf}^* distribution

The effects of using observation-based L_{cf}^* on the simulated cloud fields, based on the global distribution of L_{cf}^* for December–February (DJF, boreal winter) and June–August (JJA, boreal summer), are demonstrated in Fig. 1. Monthly variations in L_{cf}^* are shown in Fig. 2 for the following four regions with distinguishing cloud systems (Fig. 1, red squares): A: Eurasian Continent (EC); B: Equatorial Ocean (EO); C: Southern Hemisphere Ocean (SHO); and D: South America Western Pacific (SAWP). The values of L_{cf}^* were larger in the Northern Hemisphere (NH) in DJF and smaller in JJA, and the opposite trend was observed in the Southern Hemisphere (SH), as shown in Fig. 2.

Region A represents the high-latitude EC. The value of L_{cf}^* in DJF (JJA) was approximately 5–6 km (2–3 km) for this region, which is consistent with ground radar observations (Mace and Benson-Troth, 2002; Oreopoulos et al., 2012). The larger value in DJF is due to the usually stable atmosphere and thick clouds; the smaller value is associated with an unstable atmosphere and deep convection. Region B represents the tropical deep convection zone, in which clouds usually develop from the lower levels to above the tropopause (Wang et al., 1998), and the value of L_{cf}^* is generally >2 km. In region C, the L_{cf}^* decreased to 1–2 km due to the cold sea surface temperature (SST) and layered clouds
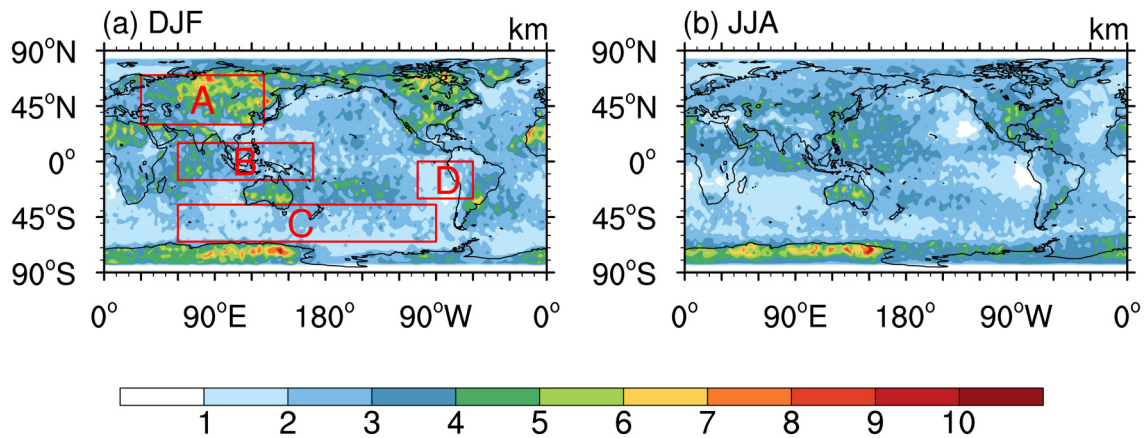
Fig. 1. The global distribution of L_{cf}^* in DJF and JJA. The four regions are designated by red squares (A:30°–70°N, 30°–130°E; B:15°S–15°N, 60°–170°E; C:65°–35°S, 60°E–90°W; D:30°S–EQ, 120°–75°W).
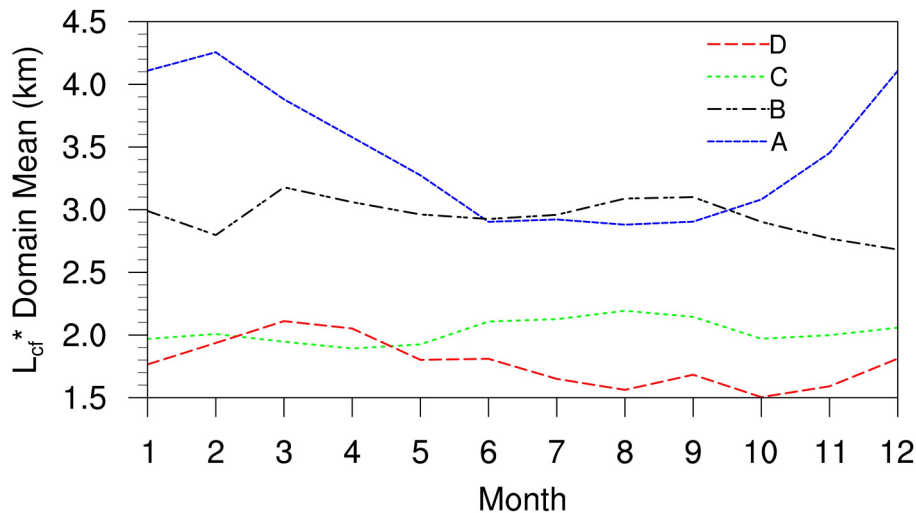
Fig. 2. Monthly changes in L_{cf}^* in four regions.

(Wood, 2012) with irregular cloud shape and limited vertical development. Region D comprises the sinking area of the Walker Circulation, giving rise to a minimum value of L_{cf}^* (<1 km) in both DJF and JJA.

3.2. *Impacts on the simulated total cloud fraction (C_{tot})*

Figure 3 shows the differences in C_{tot} between two-moment scheme simulations (EXP1 and EXP2) and CERES in DJF and JJA. Corresponding results for the one-moment scheme simulations are shown in Fig. S1 in the Electronical Supplementary Materials (ESM). In DJF, there were significant positive differences over the equatorial and mid-to-high latitude land areas and significant negative differences over the mid-latitude ocean. In JJA, however, there were

large positive biases over the near-equator ocean and negative biases over the mid-latitude ocean, especially over the Indian Peninsula and the Indian Ocean. Compared with the one-moment scheme (Fig. S1), the C_{tot} relative error associated with the two-moment simulations compared to CERES was lower by 42.9%–84.8% (Table 2). The positive biases in the equatorial region and the negative biases over the Indian Ocean were much smaller in EXP2 than in EXP4. The cloud fraction bias was generally smaller in JJA than in DJF.

According to C_{tot} differences between the simulations and CERES, C_{tot} was smaller in DJF and JJA in EXP2 compared to EXP1. The C_{tot} bias of EXP2 was higher by 6.6% and 1.64% in DJF and JJA, respectively, compared with
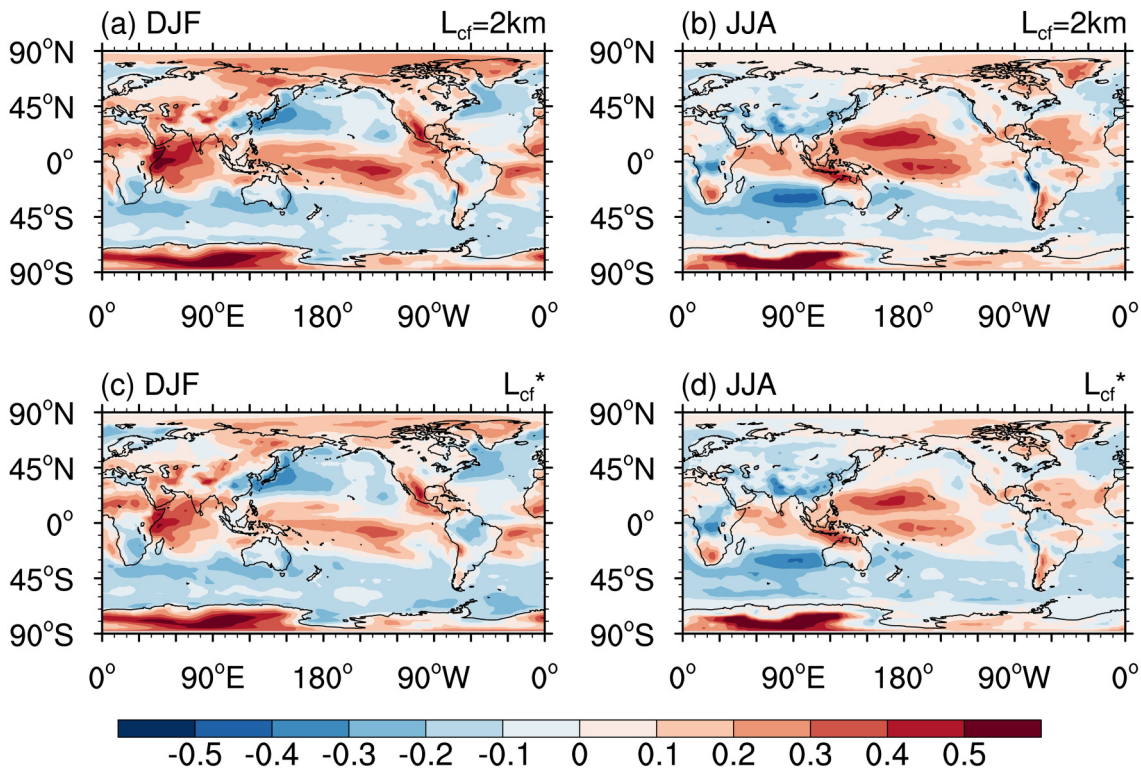
Fig. 3. Differences in the distribution of C_{tot} between simulations and CERES (EXP1,2) for two time periods, DJF and JJA.

Table 2. The C_{tot} differences between simulations and CERES for four different regions for the two time periods of DJF and JJA (unit: %) for two different observer-based cloud decorrelation lengths – fixed value (L_{cf}) and temporally/spatially varying values (L_{cf}^*).

Regions	EXP	$L_{cf} = 2$ km (DJF)	L_{cf}^* (DJF)	$L_{cf} = 2$ km (JJA)	L_{cf}^* (JJA)
Globe	EXP1/2	4.1	0.9	1.4	−0.9
	EXP3/4	7	6.6	4.3	3.9
A	EXP1/2	11.1	7	−9.5	−10.8
	EXP3/4	19.1	18.4	−8.1	−8.6
B	EXP1/2	20.2	15	20.7	15.9
	EXP3/4	16.5	15.8	18	17.3
C	EXP1/2	−12.3	−14.6	−12.2	−14.1
	EXP3/4	−9.3	−9.2	−6.5	−6.5
D	EXP1/2	3.5	1.2	−5.1	−5
	EXP3/4	4.9	5.2	−0.7	−0.2

that of EXP1 (Table 2).

In previous one-moment microphysics studies, differences between C_{tot} simulated from models and satellite data were mainly concentrated in the equatorial region and in the polar regions (Fig. S2). By contrast, the differences between the two-moment simulations and CERES were mainly concentrated in the SH (Fig. 4), most likely due to the existence of sea ice in the SH and the sophisticated mixed-phase cloud processes in the model (Tan et al., 2016; Flynn and Mauritsen, 2020). The results over the polar regions were improved by the two-moment scheme. Compared with EXP1, the biases were small at the equator for DJF and large from 30°S to the equator for JJA in EXP2. This is because L_{cf}^* is >2 km in the tropics in DJF and <2 km in the SH in JJA (Fig. 1). Compared with Wang et al. (2018), the errors of C_{tot} simulated by the new scheme are lower in zonal means using either type of cloud microphysics schemes. The observation-based L_{cf}^* reduces the cloud fraction bias more effectively in the two-moment model, especially in the equatorial and mid-to-high latitudes of the NH.

Table 2 presents the C_{tot} simulations and CERES data globally and for the four regions shown in Fig. 1, including the results of Wang et al. (2018). From a global perspective, both the two-moment scheme and the new cloud-overlap treat-ment improve the simulation accuracy of C_{tot}. In DJF (JJA), the two-moment cloud microphysics scheme contributes 9.4% (7.9%) to the improvement, and the L_{cf}^* scheme contributes 5.3% (3.8%). The improvement in region A is more evident than in the other regions in DJF, as the two-moment scheme contributes 22.1%, and the L_{cf}^* scheme contributes 7.9%. However, the results in JJA are not satisfactory. Region B is affected by equatorial deep convective clouds; thus, the simulations were biased. Jing et al. (2018) improved the L_{cf}^* scheme in the equatorial region, linking L_{cf}^* with ω_{500} to reduce errors. Region C is a marine region in the SH, as discussed earlier. The improvement in Region D in DJF is noticeable, where the two-moment method contributes 6.3%, and the L_{cf}^* scheme contributes 3.6%. Similar to Region A, the results show little improvement in JJA. In summary, the L_{cf}^* scheme improved the simulations, with the improvement more evident in the two-moment scheme than in the one-moment scheme. However, the results in the equatorial and SH marine areas remain biased and require further improvement.

3.3. Impacts on simulated cloud vertical structure

Figure 5 shows a schematic diagram of a scatter plot of N ($N = -SWCRF/LWCRF$) vs. NETCRF [NETCRF = SWCRF + LWCRF; see Zhang et al. (2020) for details]. The
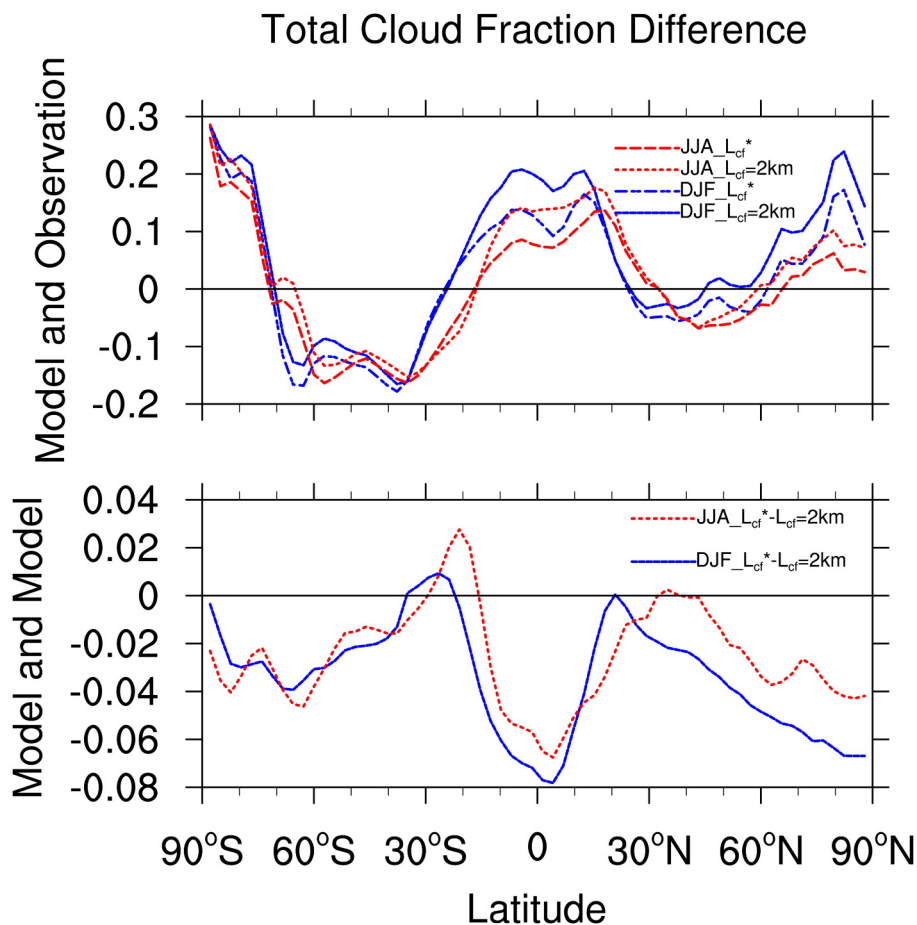
Fig. 4. Zonal means of C_{tot} differences between simulations and CERES (top) and differences in C_{tot} simulations between EXP1 and EXP2 (bottom) in DJF and JJA.

above method can be used to obtain the characteristics of cloud vertical structure, including cloud top and cloud optical thickness (Potter and Cess, 2004), to resolve the three-dimensional structure of the cloud.

Given the superiority of the two-moment cloud microphysics scheme in simulating C_{tot} as demonstrated above, we used the two-moment model to evaluate the effects of different L_{cf} treatments on the simulated cloud vertical structure and CRF. Figure 6 shows scatter plots of N vs. NETCRF to represent the vertical structure of the cloud in the four regions. The results of CERES in Region A show that the distributions in DJF are mainly concentrated in the fourth quadrant, whereas those in JJA are mainly concentrated in the second quadrant. This implies that Region A contains mostly cirrus clouds (large L_{cf}^*) in DJF and deep convective clouds (small L_{cf}^*) in JJA, which is consistent with the analysis results shown in Fig. 2. In Region A, most of the CERES data scatter in DJF appears in the area where N <2 and NETCRF < −40 W m^{-2}. Both L_{cf} treatments captured such characteristics well. However, in JJA, the CERES-based results are found in the region where N <4 and NETCRF < −80 W m^{-2}, whereas the model results rarely show NETCRF < −40 W m^{-2}, suggesting that, regardless of the L_{cf} treatments, the model underestimates SW cloud radiation flux. For Region B, the results derived from CERES were similar for DJF and JJA. The values of N calculated from both the model and CERES data were roughly less than 2. However, the simulated NETCRF, unlike the observations, were all shifted to the left, indicating that the model underestimates LW cloud radiation flux in this area, which is also consistent with Fig. 6b and 6d. For Region D, the CERES results in DJF imply that the cloud structure is a combination of middle and low clouds, with N <7.4 and NETCRF < −80 W m^{-2}.

The L_{cf}^* simulation showed clouds concentrated in the area where N <7.8 and NETCRF < −70 W m^{-2}, which is an improvement in the representation, compared with the global-constant setup.

Overall, both L_{cf} schemes roughly captured the vertical structural characteristics of cloud coverage. Nevertheless, both simulations underestimated SWCRF in Regions A, C, and D, and underestimated LWCRF in Region B. This implies that, apart from cloud overlap treatment, there are problems in other parts of the model that could lead to biases in modeled CRF.

3.4. *Impacts on simulated cloud radiative forcing (CRF)*

Figure 7 provides the probability density function (PDF) of CRF in the four regions. In DJF, the simulations and CERES are in good agreement for both the peak value and the variation range. In JJA, the CERES PDF peaks are populated by LWCRF at approximately 22 W m^{-2}. Both L_{cf} schemes succeeded in capturing the observed distributions in terms of border shapes but produced higher peaks for the LWCRF PDF. The simulation is not ideal in Region B due to deep convective clouds. The simulated LWCRF and SWCRF in Regions C and D were consistent with observation data. Moreover, the PDF peak from the simulations is very close to that of the observations in Region C in DJF (27 and 27.5 W m^{-2}, respectively). Taken together, the results show that the L_{cf}^* scheme behaves better for LWCRF in specific areas; however, the simulation of SWCRF requires further improvement.

Compared with observation data, the modeled SWCRF was underestimated in tropical convection regions and in mid-to-high latitudes in the SH (negative deviation) but overestimated in the low-latitude regions in the SH and most
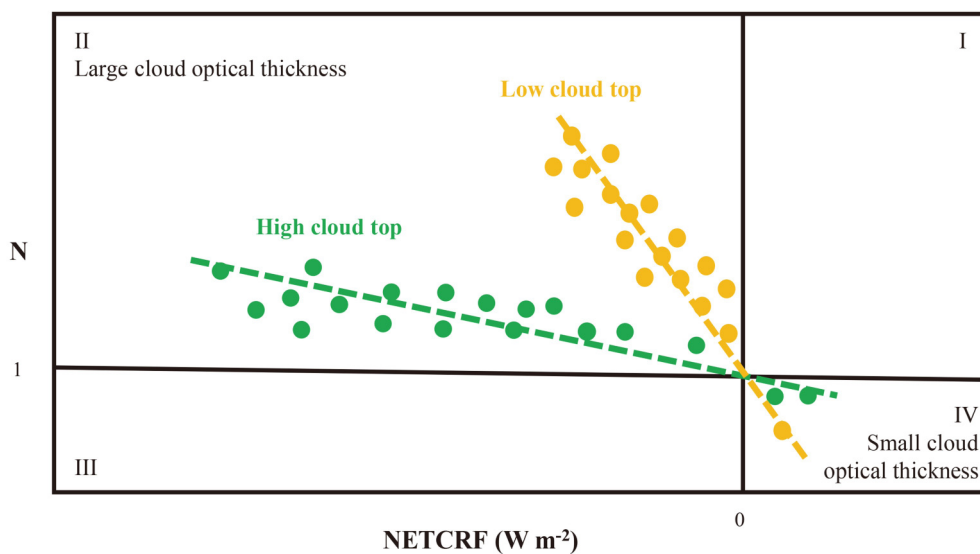
Fig. 5. Schematic scatter plot of *N* vs. NETCRF. The numbers I, II, III, and IV indicate the different quadrants, the horizontal and vertical lines indicate *N*=1 and NETCRF=0, respectively, which are indicative of an expected cancellation between the SWCRF and LWCRF. The yellow (green) dots indicate the clouds with low (high) cloud top, and the yellow (green) line is the line of best fit using a linear least squares method.
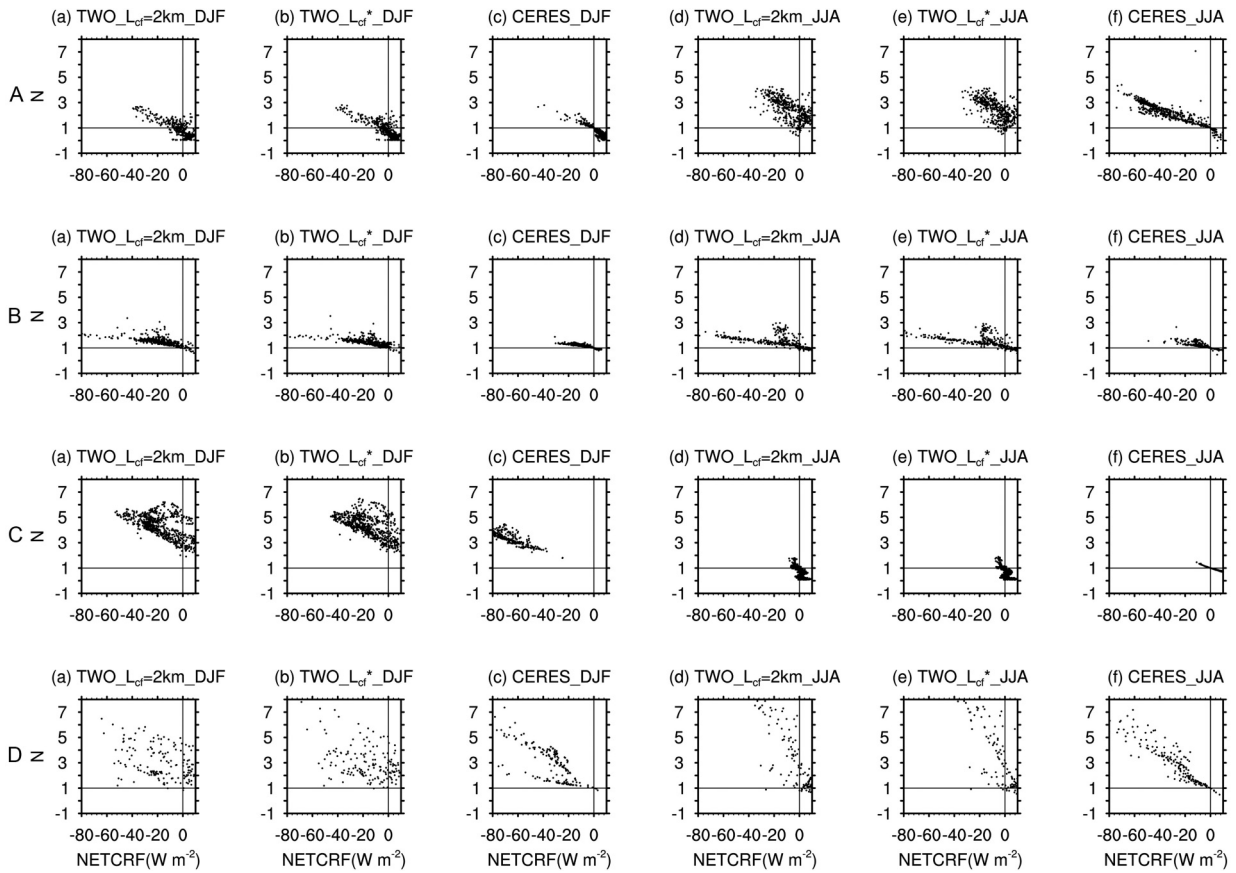
Fig. 6. Scatter plots of N vs. NETCRF in A, B, C and D areas: (a–c) DJF, (d–f) JJA, (a, d) L_{cf} =2 km, (b, e) L_{cf}^*, (c, f) CERES.
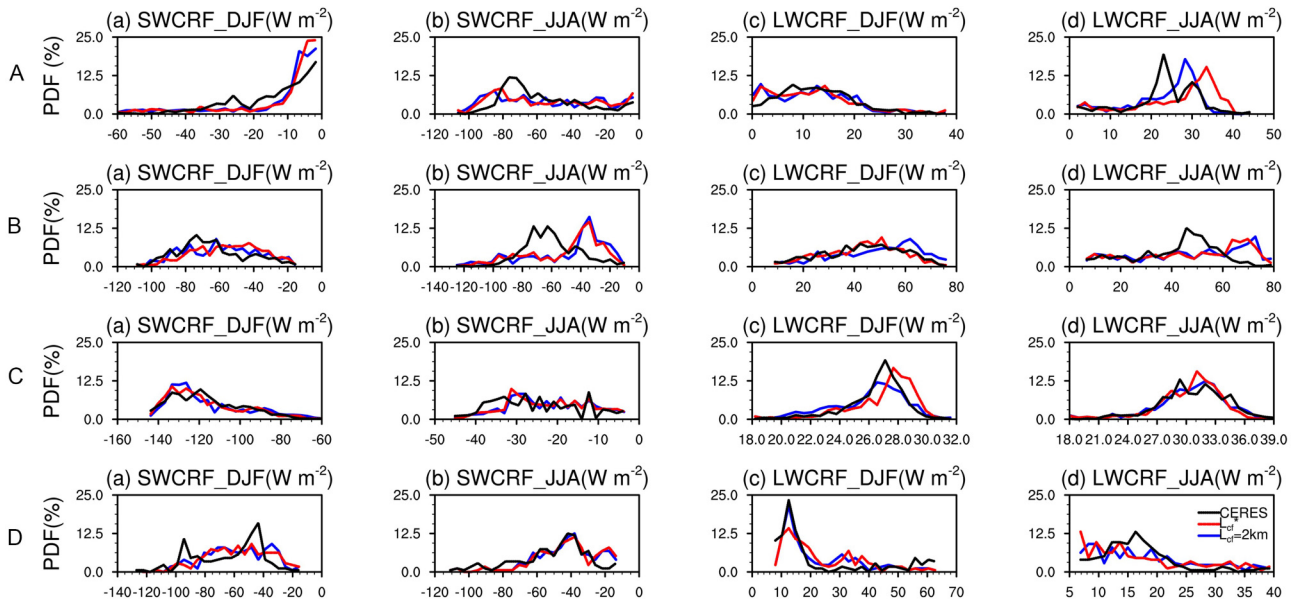
Fig. 7. The probability distribution of CRF in four regions A, B, C, and D. Individual panels depict: (a) SWCRF in DJF, (b) SWCRF in JJA, (c) LWCRF in DJF, and (d) LWCRF in JJA. The black, red and blue lines represent the results of CERES, the new scheme, and the old scheme respectively).

parts of the NH (positive deviation), as shown in Fig. 8. In DJF, the L_{cf}^* scheme reduced the SWCRF in the low-latitude regions of the SH and increased the SWCRF in equatorial regions, indicating an improvement in SWCRF relative to the global constant L_{cf}. In JJA, negative biases were significant in the tropical convective area (especially in South Asia and the central-eastern subtropical Pacific) and at high latitudes near 60°N (Figs. 6b, d), with NETCRF exceeding
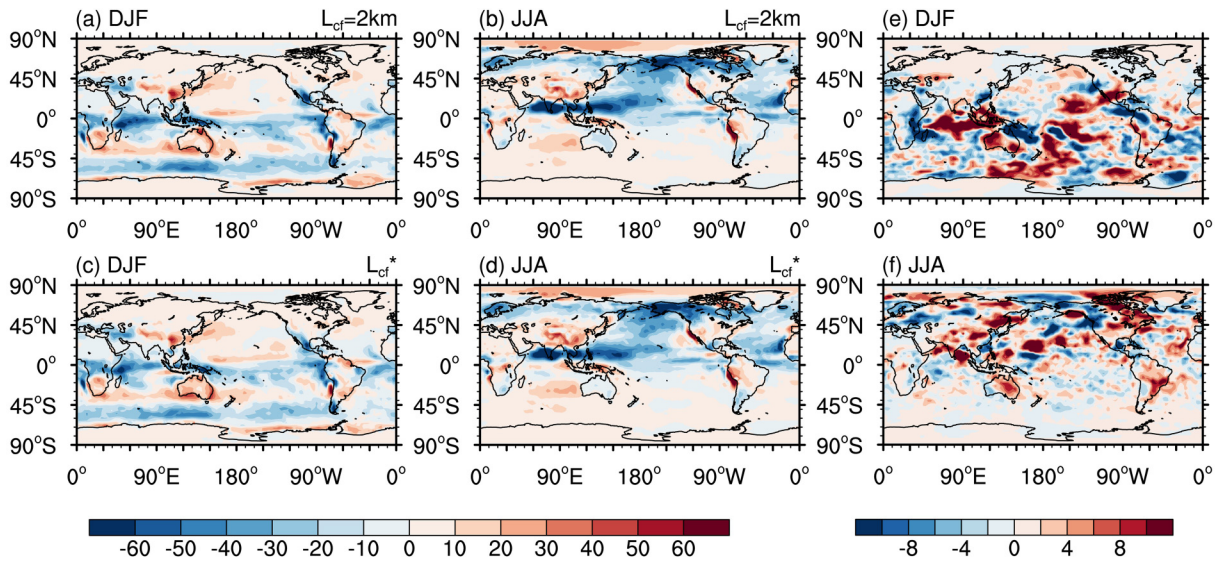
Fig. 8. Differences in the distribution of SWCRF between simulations and CERES (a-d) for two time periods, in DJF and JJA; and differences in the distribution of SWCRF between simulations (e-f) for DJF and JJA for two different observer-based cloud decorrelation lengths – fixed value (L_{cf}) and temporally/spatially varying values (L_{cf}*). (unit: W m^{-2}).

−50 W m^{-2}. In the L_{cf}* schemes, the simulations errors in the areas mentioned above were significantly reduced compared with results from the old scheme (Figs. 8e, f).

Similar improvements could also be seen in the simulation of LWCRF (Fig. 9). The L_{cf}* scheme reduced the overestimation (underestimation) of the LWCRF in the western tropical and central Pacific regions (high-latitude ocean of the SH) in DJF. Moreover, it also reduced the overestimation of LWCRF in the tropical central region in JJA. The reduction in these deviations was within ±5 W m^{-2}, which is approximately an order of magnitude smaller than the difference between the simulations and satellite data.

The improvements in SWCRF and LWCRF correspond to an improvement in the simulated C_{tot} (Fig. 3), indicating that cloud fraction can affect CRF. The improvement in the

L_{cf}* scheme in many regions shows that at least part of the deviation in the GCM's radiation budget can be attributed to the treatment of cloud overlap.

According to Eqs. (3) and (4), CRF is the joint result of an all-sky term (Figs. 10a, b) and a clear-sky term. Figure 10 shows the impacts of the two L_{cf} treatments on these two terms, respectively. The differences in CRF caused by both L_{cf} schemes were mainly noticeable under all-sky conditions. The differences in CRF of the all-sky shortwave radiant flux obtained by the model was largest in the equatorial region in DJF and in the middle and high latitudes of the NH in JJA. Differences in the all-sky longwave radiant flux exhibited an oscillating trend, with no discernible change characteristics. The influence on the clear-sky shortwave radiant flux was more pronounced in the NH than in other regions
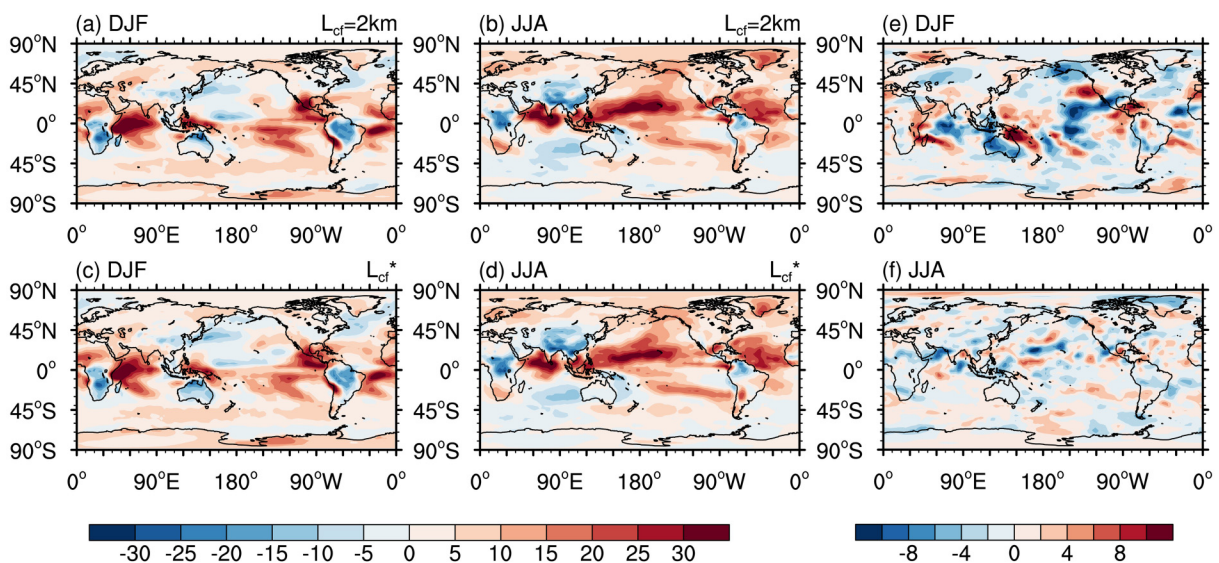
Fig. 9. Same as Fig. 8. but for LWCRF (units: W m^{-2}).
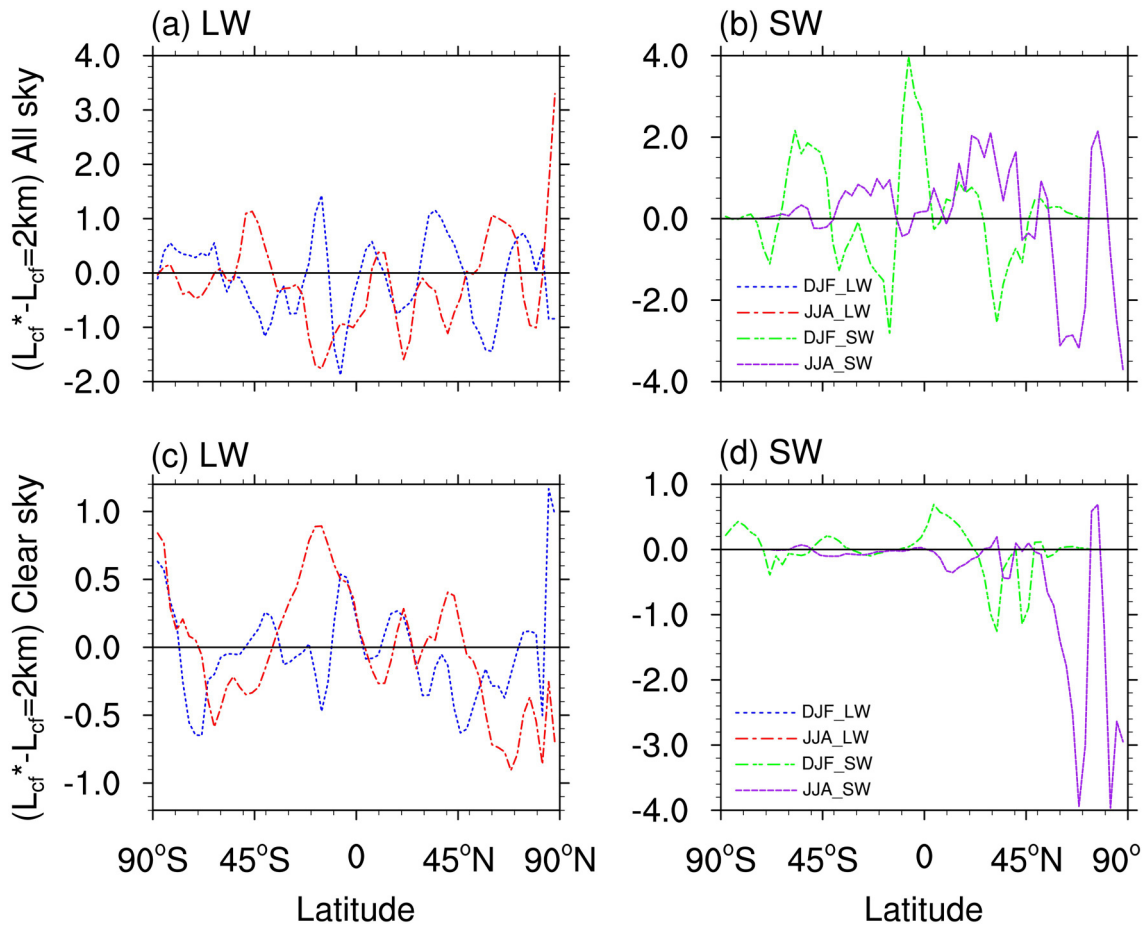
Fig. 10. Zonal means of simulated radiation flux difference (unit: W m^{-2}): (a) all-sky-LW, (b) all-sky-SW, (c) clear-sky-LW, (d) clear-sky-SW.

in JJA.

For SWCRF, the L_{cf}^* scheme improved the simulations on a global basis by 0.3% and 1.2% in DJF and JJA, respectively (Table 3). The biases in SWCRF in Region A were reduced by 1.1% in DJF. The SWCRF and LWCRF simulations were not ideal in Region C, where the ocean dominates. Region B (D) exhibited an improvement of 5.4% (0.2%) and 0.7% (0.6%) in DJF and JJA, respectively. Similarly, for LWCRF, global simulations improved under the L_{cf}^* scheme, by 0.8% and 1.2% in DJF and JJA, respectively. The accuracy in Region A (C) increased by 4.5%

(2.0%), while that in Region B (D) improved by 1.9% (1.2%) and 1.1% (0.5%) in DJF and JJA, respectively. Taken together, these results emphasize the importance of representing the regional variation in L_{cf} to provide a more accurate representation of the regional radiation budget.

4. Analysis and discussion

The formation, evolution, and distribution of clouds are mainly determined by atmospheric circulation, the land–sea distribution, local thermal radiative heating (Mather et al.,

Table 3. The Cloud Radiation Forcing (CRF) differences between simulations and CERES for four different regions and two time periods DJF and JJA for two different observer-based cloud decorrelation lengths – fixed value (L_{cf}) and temporally/spatially varying values (L_{cf}^*).

CRF	Model Parameter	Globe		A		B		C		D	
		DJF	JJA	DJF	JJA	DJF	JJA	DJF	JJA	DJF	JJA
CRF$_S$ (W m^{-2})	L_{cf} = 2 km	4.24	5.64	−0.51	−1.11	16.4	16.57	6.89	−3.46	11.24	−8.03
	L_{cf}^*	4.06	5.09	−0.69	−1.75	12.9	16.13	11.47	−3.28	11.1	−8.34
CRF$_L$ (W m^{-2})	L_{cf} = 2 km	4.95	5.05	2.5	−1.44	9.98	13.65	4.92	1.29	5.68	2.26
	L_{cf}^*	4.75	4.76	1.89	−1.7	9.15	13.19	4.4	1.61	5.4	2.17

2007; Klinger et al., 2019) and topographic lifting (Sato et al., 2007; Kumar et al., 2019). Many other factors, including aerosols, cloud condensation nuclei/ ice nuclei, and water vapor, etc., are also closely associated with the development of clouds through thermal, dynamic, and cloud microphysical processes (Yang et al., 2019; Zhao et al., 2020). The interactions among different processes are complex. Changes in these processes affect the radiative properties of clouds.

4.1. Surface temperature and circulation

Figure 11 shows the differences in the wind field and surface temperature in the one-moment/two-moment experiments (two-moment – one-moment) under the same cloud overlapping scheme in DJF and JJA. Changes in surface temperature affect clouds in various ways. First, surface temperature influences the water vapor content in the atmosphere through modulation of surface evaporation. Specifically, a higher surface temperature implies a higher efficiency of evaporation of water vapor from the surface and vice versa. Under the same temperature and pressure, increased water vapor in the atmosphere facilitates cloud formation. Second, changes in air temperature can change the stability of the atmosphere. When the temperature increases at lower levels, the stability of the atmosphere will decrease, and convective activities are more likely to occur, which can promote the formation and development of clouds. On the contrary, colder low-level temperatures tend to stabilize the atmosphere and decrease the cloud fraction.

For both cloud overlapping treatments, the surface temperature simulated by the two-moment scheme was colder in the polar regions compared to that in the one-moment simulations, which inhibits the formation of clouds. These changes brought by the two-moment scheme helped to reduce the positive bias associated with the cloud fraction in the polar regions (Fig. S1). Consequently, the reduction in the cloud fraction bias was more substantial than in the two-moment scheme. Furthermore, the surface temperature decreased more under the L_{cf}^* scheme than under the old L_{cf} scheme. Similarly, the model performance also improved over the mid-latitude oceans of the SH, East Asia, and North America for DJF and for the mid-latitude oceans of the SH and South America for JJA. For atmospheric circulation, taking the European continent in DJF as an example, the movement of the circulation to the northwest is related to the decrease in total cloud fraction. Compared with Fig. S1, it is found that the L_{cf}^* produces an improvement in the total cloud fraction, which reduces the positive deviation.

Figure 12 shows the differences in wind and surface temperature between the L_{cf}^* and old L_{cf} schemes. In the two-moment model, the surface temperature differences between the two schemes were negative in DJF for the Eurasian continent and North America, which indicate inhibition of cloud formation and imply an improvement compared with the results in Fig. 3. In DJF, simulations of the northern and southern ocean surfaces were reversed. Compared with Figs. 12a and 12c, the differences in surface temperature simulated
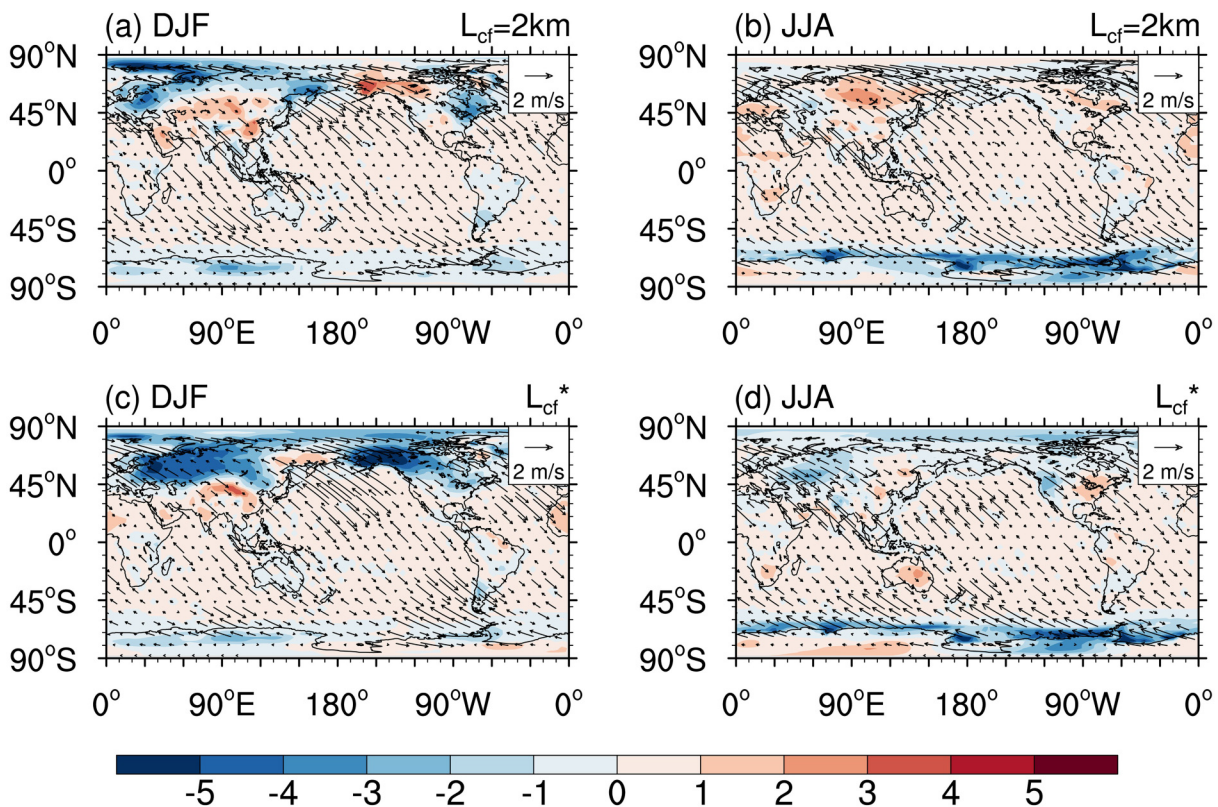
Fig. 11. Differences in surface wind field (arrows) and surface temperature (shaded; °C) between different cloud microphysical schemes (a–b: EXP1–EXP3; c–d: EXP2–EXP4) for two time periods, in DJF and JJA.
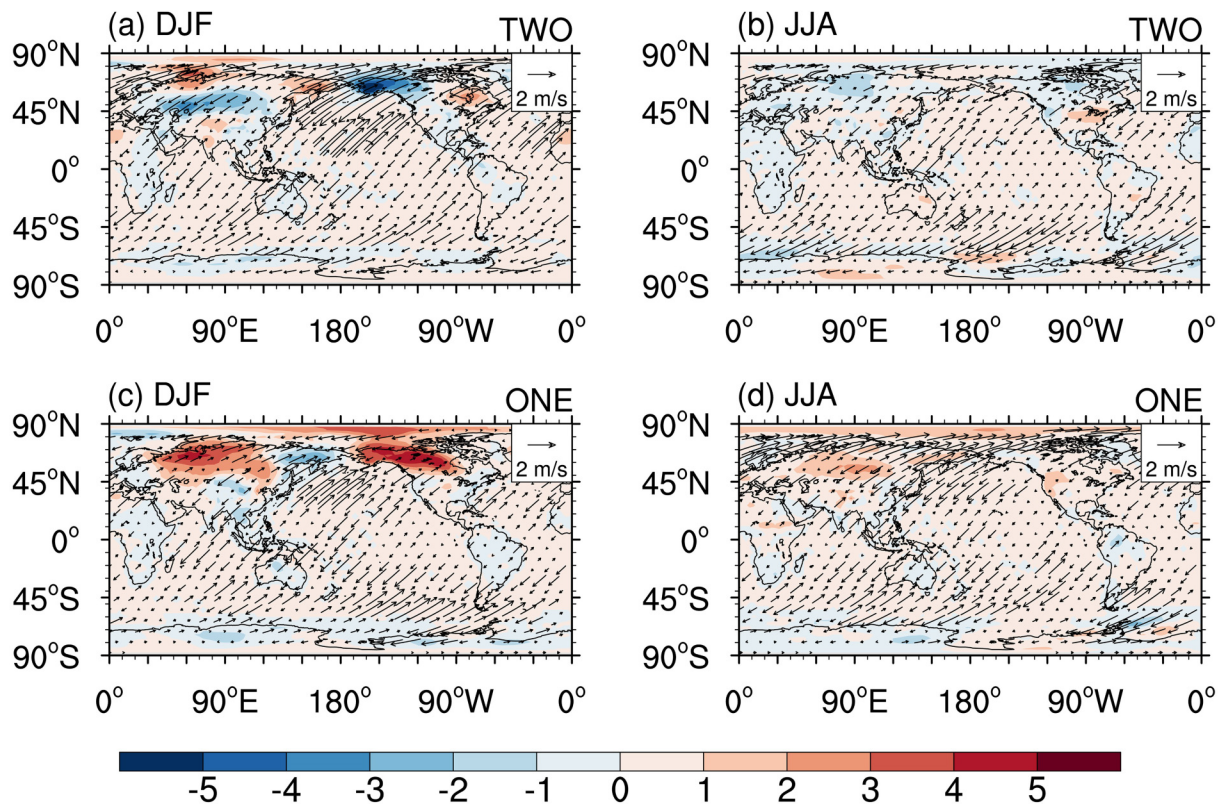
Fig. 12. Differences in surface wind field (arrows) and surface temperature (shaded; °C) between different cloud overlap treatments (a–b: EXP1-EXP2; c–d: EXP3-EXP4) for two time periods, in DJF and JJA.

by the two-moment model were negative in central Europe and northern North America in DJF, which also suggests the suppression of cloud formation and an improvement compared with observation data. Similarly, taking the European continent in DJF as an example, the movement of the circulation to the southwest is manifested as a decrease in total cloud fraction. Compared with Fig. S1, it is found that the results of the two-moment cloud microphysics scheme can offset the positive deviation in this area.

However, the differences in surface temperature simulated by the one-moment scheme were positive, which indicate the promotion of cloud formation and an increase in the simulation error. Thus, simulations using the two-moment model have advantages in certain areas. The same is true in JJA.

4.2. *Relative humidity*

Figure 13 shows that the relative humidity increased between 30°S and 60°S in DJF, which is conducive to cloud formation. A comparison made with Fig. 3 and Fig. S1 shows that the two-moment simulations improved the underestimation of cloud fraction in these areas. The relative humidity of the entire layer between 30°S and 60°S in DJF (Fig. 13) is indicative of enhanced water vapor, which is favorable for cloud formation. Using the L_{cf}^{*} scheme, the relative humidity increased over a wider convergence area, which reflects the superiority of the L_{cf}^{*} scheme in these

regions. The same effect was found on both sides of the equator, as well as in the mid-to-high latitudes of the NH. The same is true in JJA.

In DJF, the relative humidity between 35°S and 45°S increased in the whole layer (Fig. 14) which is conducive to the formation of clouds. These features of the two-moment simulations can reduce the underestimation of the cloud fraction in the above area. Similarly, in JJA, the relative humidity simulated by the two-moment scheme between 45°N and 60°N increased, which is indicative of the promotion of cloud formation and a reduction in error for the simulated cloud fraction. In summary, the advantage of the L_{cf}^{*} treatment manifests itself more prominently in the two-moment microphysics scheme than in the one-moment model.

5. Summary

The interaction between clouds and climate through microphysical and radiative processes is one of the most crucial factors leading to simulation uncertainties. In this study, the effects of cloud microphysics schemes (one-moment vs. two-moment) and cloud overlap methods (fixed value vs. observation-based vertical decorrelation length) on the simulated cloud fraction and associated meteorological conditions were evaluated in detail using the BCC_AGCM2.0_CUACE/Aero model. The main conclusions are as follows:

a) Regarding the effects of cloud overlap treatments,
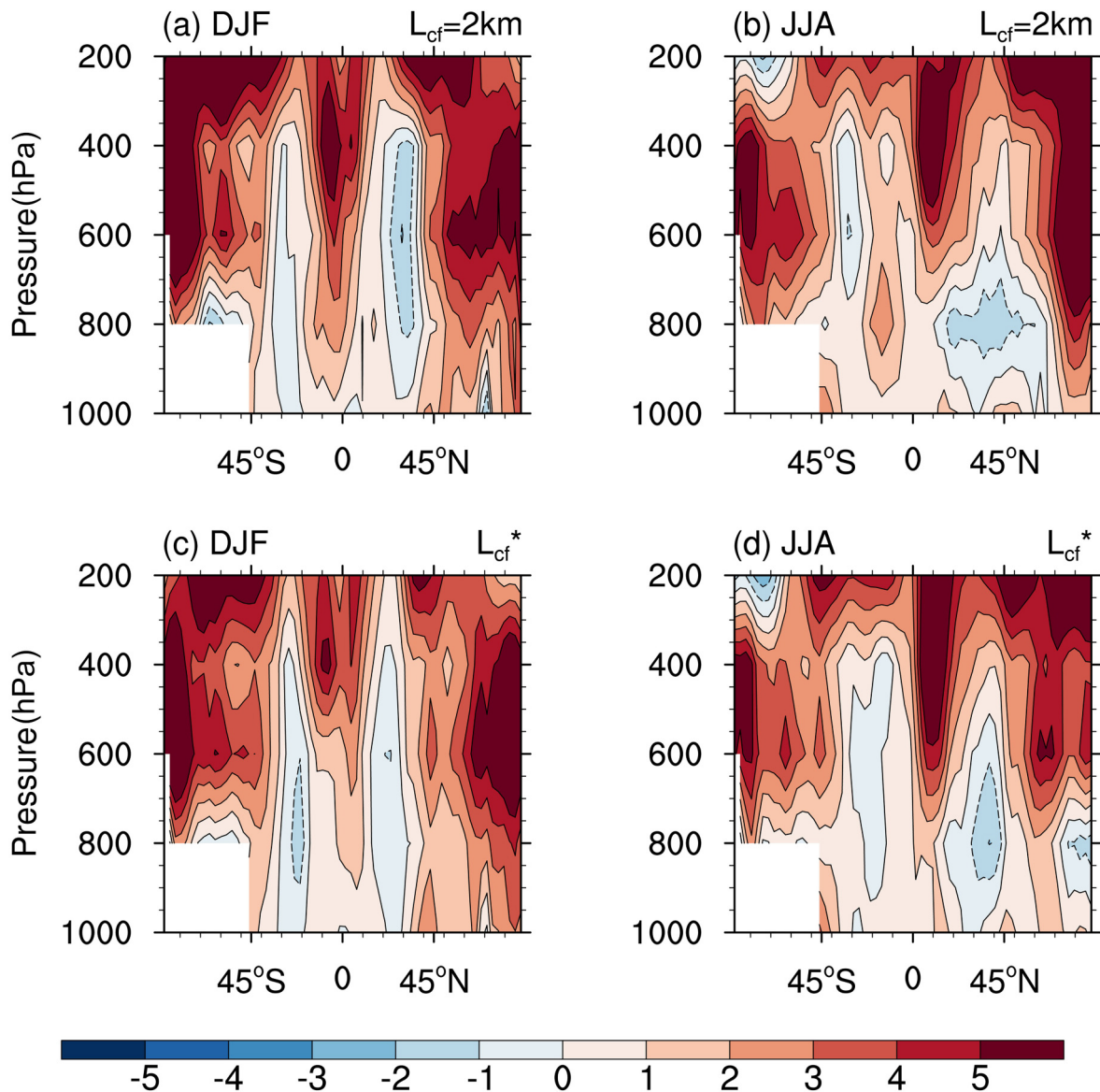
Fig. 13. Same as Fig. 11, but for the vertical distribution of relative humidity (unit: %).

the cloud-related variables simulated by the model utilizing observation-based vertical decorrelation length (new scheme) were improved significantly, whether in the global mean sense or for the selected four representative regions. Compared with the findings of Wang et al. (2018), the new scheme utilizing the two-moment model resulted in better simulation accuracy of C_{tot} compared with that using the one-moment scheme.

b) The improved C_{tot} simulation improved the accuracy of energy budget simulations in different regions. The simulated CRF globally and in the four regions improved by 0.3% –1.2% and 0.2%–2.0%, respectively. The effect on CRF mainly stems from the cloudy atmosphere, with the effect on SW radiation being more significant than that on LW radiation.

c) Both L_{cf} treatments can capture the vertical structural characteristics of clouds. The model performance was best

for Region D among the four regions studied. The underestimation of SWCRF was evident in the other regions (A, C, and D), indicating that the L_{cf} value must be designated for a specific region.

Therefore, describing the vertical structure of clouds using L_{cf}^{*} obtained from CloudSat/CALIPSO can significantly improve the simulation of cloud-related variables in the BCC_AGCM2.0_CUACE/Aero model, especially when two-moment microphysics is used. Nevertheless, large regional biases in cloud fraction still exist, regardless of the cloud overlap and microphysical treatments, implying other underlying issues in the model. In future research, our efforts will focus on providing a more realistic representation of the spatiotemporal variation in cloud overlap in the model, as well as addressing other associated issues, to improve the simulation of radiation budget variations.
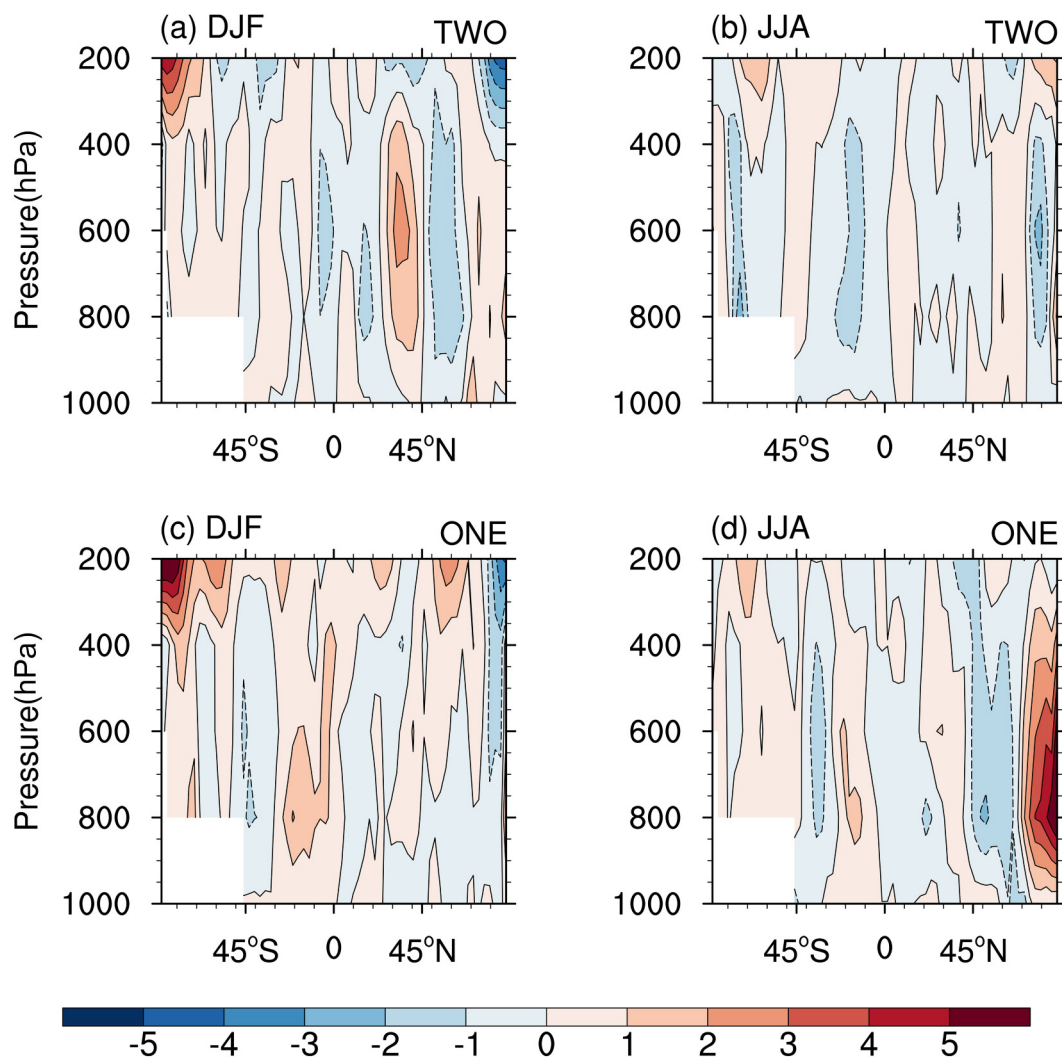
Fig. 14. Same as Fig. 12. but for vertical distribution of relative humidity (units: %).

REFERENCES

Barker, H. W., 2008: Overlap of fractional cloud for radiation calculations in GCMs: A global analysis using CloudSat and CALIPSO data. *J. Geophys. Res. Atmos.*, **113**, D00A01, https://doi.org/10.1029/2007JD009677.

Barker, H. W., G. L. Stephens, and Q. Fu, 1999: The sensitivity of domain-averaged solar fluxes to assumptions about cloud geometry. *Quart. J. Roy. Meteor. Soc.*, **125**, 2 127−2 152, https://doi.org/10.1002/qj.49712555810.

Bergman, J. W., and P. J. Rasch, 2002: Parameterizing vertically coherent cloud distributions. *J. Atmos. Sci.*, **59**, 2 165−2 182, https://doi.org/10.1175/1520-0469(2002)059<2165:PVCCD >2.0.CO;2.

Collins, W. D., and Coauthors, 2004: Description of the NCAR community atmosphere model (CAM 3.0). NCAR Tech. Note NCAR/TN-464+STR, 226 pp, https://doi.org/10.5065/D63N21CH.

Di Giuseppe, F., 2005: Sensitivity of one-dimensional radiative biases to vertical cloud-structure assumptions: Validation with aircraft data. *Quart. J. Roy. Meteor. Soc.*, **131**, 1 655−1 676, https://doi.org/10.1256/qj.03.129.

Di Giuseppe, F., and A. M. Tompkins, 2015: Generalizing cloud overlap treatment to include the effect of wind shear. *J. Atmos. Sci.*, **72**, 2 865−2 876, https://doi.org/10.1175/JAS-D-14-0277.1.

Ding, S. G., C. S. Zhao, G. Y. Shi, and C. A. Wu, 2005: Analysis of global total cloud amount variation over the past 20 years. *Journal of Applied Meteorological Science*, **16**, 670−677, https://doi.org/10.3969/j.issn.1001-7313.2005.05.014. (in Chinese with English abstract)

Fan, T. Y., and Coauthors, 2018: Quantify contribution of aerosol errors to cloud fraction biases in CMIP5 Atmospheric Model Intercomparison Project simulations. *International Journal of Climatology*, **38**, 3 140−3 156, https://doi.org/10.1002/joc.5490.

Flynn, C. M., and T. Mauritsen, 2020: On the climate sensitivity and historical warming evolution in recent coupled model ensembles. *Atmospheric Chemistry and Physics*, **20**, 7 829–7 842, https://doi.org/10.5194/acp-20-7829-2020.

Garrett, T. J., and C. F. Zhao, 2006: Increased Arctic cloud long-wave emissivity associated with pollution from mid-latitudes. *Nature*, **440**, 787–789, https://doi.org/10.1038/nature 04636.

Ghan, S. J., L. R. Leung, and Q. Hu, 1997: Application of cloud microphysics to NCAR community climate model. *J. Geophys. Res. Atmos.*, **102**, 16 507–16 527, https://doi.org/10.1029/97JD00703.

Ghan, S. J., X. Liu, R. C. Easter, R. Zaveri, P. J. Rasch, J.-H. Yoon, and B. Eaton, 2012: Toward a minimal representation of aerosols in climate models: Comparative decomposition of aerosol direct, semidirect, and indirect radiative forcing. *J. Climate*, **25**, 6 461–6 476, https://doi.org/10.1175/JCLI-D-11-00650.1.

Harrison, E. F., P. Minnis, B. R. Barkstrom, V. Ramanathan, R. D. Cess, and G. G. Gibson, 1990: Seasonal variation of cloud radiative forcing derived from the Earth Radiation Budget Experiment. *J. Geophys. Res. Atmos.*, **95**, 18 687–18 703, https://doi.org/10.1029/JD095iD11p18687.

Hogan, R. J., and A. J. Illingworth, 2000: Deriving cloud overlap statistics from radar. *Quart. J. Roy. Meteor. Soc.*, **126**, 2 903–2 909, https://doi.org/10.1002/qj.49712656914.

Intergovernmental Panel on Climate Change, 2013: *Climate Change 2013: The Physical Science Basis*. Cambridge University Press, 1535 pp.

Jing, X. W., H. Zhang, J. Peng, J. N. Li, and H. W. Barker, 2016: Cloud overlapping parameter obtained from CloudSat/CALIPSO dataset and its application in AGCM with McICA scheme. *Atmospheric Research*, **170**, 52–65, https://doi.org/10.1016/j.atmosres.2015.11.007.

Jing, X. W., H. Zhang, M. Satoh, and S. Y. Zhao, 2018: Improving representation of tropical cloud overlap in GCMs based on cloud-resolving model data. *J. Meteor. Res.*, **32**, 233–245, https://doi.org/10.1007/s13351-018-7095-9.

Kato, S., S. Sun‐Mack, W. F. Miller, F. G. Rose, Y. Chen, P. Minnis, and B. A. Wielicki, 2010: Relationships among cloud occurrence frequency, overlap, and effective thickness derived from CALIPSO and CloudSat merged cloud vertical profiles. *J. Geophys. Res. Atmos.*, **115**, D00H28, https://doi.org/10.1029/2009JD012277.

Klinger, C., G. Feingold, and T. Yamaguchi, 2019: Cloud droplet growth in shallow cumulus clouds considering 1-D and 3-D thermal radiative effects. *Atmospheric Chemistry and Physics*, **19**, 6 295–6 313, https://doi.org/10.5194/acp-19-6295-2019.

Kumar, S., Y.-S. Vidal, A. S. Moya-Álvarez, and D. Martínez-Castro, 2019: Effect of the surface wind flow and topography on precipitating cloud systems over the Andes and associated Amazon basin: GPM observations. *Atmospheric Research*, **225**, 193–208, https://doi.org/10.1016/j.atmosres.2019.03.027.

Li, J. M., Q. Y. Lv, B. D. Jian, M. Zhang, C. F. Zhao, Q. Fu, K. Kawamoto, and H. Zhang, 2018: The impact of atmospheric stability and wind shear on vertical cloud overlap over the Tibetan Plateau. *Atmospheric Chemistry and Physics*, **18**, 7 329–7 343, https://doi.org/10.5194/acp-18-7329-2018.

Li, J. M., B. D. Jian, C. F. Zhao, Y. X. Zhao, J. Wang, and J. P. Huang, 2019: Atmospheric instability dominates the long‐term variation of cloud vertical overlap over the southern

great plains site. *J. Geophys. Res. Atmos.*, **124**, 9 691–9 701, https://doi.org/10.1029/2019JD030954.

Loeb, N. G., and Coauthors, 2018: Clouds and the Earth's radiant energy system (CERES) energy balanced and filled (EBAF) top-of-atmosphere (TOA) edition-4.0 data product. *J. Climate*, **31**, 895–918, https://doi.org/10.1175/JCLI-D-17-0208.1.

Lohmann, U., P. Stier, C. Hoose, S. Ferrachat, S. Kloster, E. Roeckner, and J. Zhang, 2007: Cloud microphysics and aerosol indirect effects in the global climate model ECHAM5-HAM. *Atmospheric Chemistry and Physics*, **7**, 3 425–3 446, https://doi.org/10.5194/acp-7-3425-2007.

Lu, P., H. Zhang, and J. N. Li, 2011: Correlated *k*-distribution treatment of cloud optical properties and related radiative impact. *J. Atmos. Sci.*, **68**, 2 671–2 688, https://doi.org/10.1175/JAS-D-10-05001.1.

Lu, R. Y., B. W. Dong, R. D. Cess, and G. L. Potter, 2004: The 1997/98 El Niño: A test for climate models. *Geophys. Res. Lett.*, **31**, L12216, https://doi.org/10.1029/2004GL019956.

Ma, Z. S., Q. J. Liu, C. F. Zhao, X. S. Shen, Y. Wang, J. H. Jiang, Z. Li, and Y. Yung, 2018: Application and evaluation of an explicit prognostic cloud‐cover scheme in GRAPES global forecast system. *Journal of Advances in Modeling Earth Systems*, **10**, 652–667, https://doi.org/10.1002/2017MS001234.

Mace, G. G., and S. Benson-Troth, 2002: Cloud-layer overlap characteristics derived from long-term cloud radar data. *J. Climate*, **15**, 2 505–2 515, https://doi.org/10.1175/1520-0442 (2002)015<2505:CLOCDF>2.0.CO;2.

Mather, J. H., S. A. McFarlane, M. A. Miller, and K. L. Johnson, 2007: Cloud properties and associated radiative heating rates in the tropical western Pacific. *J. Geophys. Res. Atmos.*, **112**, D05201, https://doi.org/10.1029/2006JD007555.

Minnis, P., D. Doelling, L. Nguyen, R. Palikonda, D. A. Spangenberg, G. Hong, and H. Yi, 2011: Improved cloud and surface properties by combining conventional and L-1 satellite imager data. Preprints, AGU Fall Meeting 2011, San Francisco, CA, USA.

Morrison, H., and A. Gettelman, 2008: A new two-moment bulk stratiform cloud microphysics scheme in the Community Atmosphere Model, version 3 (CAM3). Part I: Description and numerical tests. *J. Climate*, **21**, 3 642–3 659, https://doi.org/10.1175/2008JCLI2105.1.

Naud, C. M., A. Del Genio, G. G. Mace, S. Benson, E. E. Clothiaux, and P. Kollias, 2008: Impact of dynamics and atmospheric state on cloud vertical overlap. *J. Climate*, **21**, 1 758–1 770, https://doi.org/10.1175/2007JCLI1828.1.

Nenes, A., and J. H. Seinfeld, 2003: Parameterization of cloud droplet formation in global climate models. *J. Geophys. Res. Atmos.*, **108**, 4415, https://doi.org/10.1029/2002JD002911.

Oreopoulos, L., D. Lee, Y. C. Sud, and M. J. Suarez, 2012: Radiative impacts of cloud heterogeneity and overlap in an atmospheric General Circulation Model. *Atmospheric Chemistry and Physics*, **12**, 9 097–9 111, https://doi.org/10.5194/acp-12-9097-2012.

Pincus, R., H. W. Barker, and J.-J. Morcrette, 2003: A fast, flexible, approximate technique for computing radiative transfer in inhomogeneous cloud fields. *J. Geophys. Res. Atmos.*, **108**, 4376, https://doi.org/10.1029/2002JD003322.

Potter, G. L., and R. D. Cess, 2004: Testing the impact of clouds on the radiation budgets of 19 atmospheric general circulation models. *J. Geophys. Res. Atmos.*, **109**, D02106, https://doi.org/10.1029/2003JD004018.

Räisänen, P., and H. W. Barker, 2004: Evaluation and optimization

of sampling errors for the Monte Carlo Independent Column Approximation. *Quart. J. Roy. Meteor. Soc.*, **130**, 2 069–2 085, https://doi.org/10.1256/qj.03.215.

Räisänen, P., H. W. Barker, M. F. Khairoutdinov, J. N. Li, and D. A. Randall, 2004: Stochastic generation of subgrid-scale cloudy columns for large-scale models. *Quart. J. Roy. Meteor. Soc.*, **130**, 2 047–2 067, https://doi.org/10.1256/qj.03.99.

Randles, C. A., and Coauthors, 2013: Intercomparison of shortwave radiative transfer schemes in global aerosol modeling: Results from the AeroCom Radiative Transfer Experiment. *Atmospheric Chemistry and Physics*, **13**, 2 347–2 379, https://doi.org/10.5194/acp-13-2347-2013.

Rasch, P. J., and J. E. Kristjánsson, 1998: A comparison of the CCM3 model climate using diagnosed and predicted condensate parameterizations. *J. Climate*, **11**, 1 587–1 614, https://doi.org/10.1175/1520-0442(1998)011<1587:ACOTCM>2.0.CO;2.

Sato, T., F. Kimura, and A. S. Hasegawa, 2007: Vegetation and topographic control of cloud activity over arid/semiarid Asia. *J. Geophys. Res. Atmos.*, **112**, D24109, https://doi.org/10.1029/2006JD008129.

Shonk, J. K. P., R. J. Hogan, J. M. Edwards, and G. G. Mace, 2010: Effect of improving representation of horizontal and vertical cloud structure on the Earth's global radiation budget. Part I: Review and parametrization. *Quart. J. Roy. Meteor. Soc.*, **136**, 1 191–1 204, https://doi.org/10.1002/qj.647.

Stephens, G. L., and Coauthors, 2008: CloudSat mission: Performance and early science after the first year of operation. *J. Geophys. Res. Atmos.*, **113**, D00A18, https://doi.org/10.1029/2008JD009982.

Tan, I., T. Storelvmo, and M. D. Zelinka, 2016: Observational constraints on mixed-phase clouds imply higher climate sensitivity. *Science*, **352**, 224–227, https://doi.org/10.1126/science.aad5300.

Tompkins, A. M., and F. Di Giuseppe, 2015: An interpretation of cloud overlap statistics. *J. Atmos. Sci.*, **72**, 2 877–2 889, https://doi.org/10.1175/JAS-D-14-0278.1.

Wang, H. B., H. Zhang, X. W. Jing, and B. Xie, 2018: Effects of different cloud overlapping parameters on simulated total cloud fraction over the globe and East Asian region. *Acta Meteorologica Sinica*, **76**, 767–778, https://doi.org/10.11676/qxxb2018.027. (in Chinese with English abstract)

Wang, P.-H., P. Minnis, M. P. McCormick, G. S. Kent, G. K. Yue, D. F. Young, and K. M. Skeens, 1998: A study of the vertical structure of tropical (20°S–20°N) optically thin clouds from SAGE II observations. *Atmospheric Research*, **47–48**, 599–614, https://doi.org/10.1016/S0169-8095(97)00085-9.

Wang, Z. L., H. Zhang, and P. Lu, 2014: Improvement of cloud microphysics in the aerosol-climate model BCC_AGCM 2.0.1 _CUACE/Aero, evaluation against observations, and updated aerosol indirect effect. *J. Geophys. Res. Atmos.*, **119**, 8 400–8 417, https://doi.org/10.1002/2014JD021886.

Webb, M., C. Senior, S. Bony, and J.-J. Morcrette, 2001: Combining ERBE and ISCCP data to assess clouds in the Hadley Centre, ECMWF and LMD atmospheric climate models. *Climate Dyn.*, **17**, 905–922, https://doi.org/10.1007/s003820100157.

Wood, R., 2012: Stratocumulus clouds. *Mon. Wea. Rev.*, **140**, 2 373–2 423, https://doi.org/10.1175/MWR-D-11-00121.1.

Xie, S. C., X. H. Liu, C. F. Zhao, and Y. Y. Zhang, 2013: Sensitivity of CAM5-simulated arctic clouds and radiation to ice nucleation parameterization. *J. Climate*, **26**, 5 981–5 999, https://doi.org/10.1175/JCLI-D-12-00517.1.

Yang, Y., and Coauthors, 2019: Toward understanding the process-level impacts of aerosols on microphysical properties of shallow cumulus cloud using aircraft observations. *Atmospheric Research*, **221**, 27–33, https://doi.org/10.1016/j.atmosres.2019.01.027.

Zhang, B. C., Z. Guo, X. L. Chen, T. J. Zhou, X. Y. Rong, and J. Li, 2020: Responses of cloud-radiative forcing to strong El Niño events over the western Pacific warm pool as simulated by CAMS-CSM. *J. Meteor. Res.*, **34**, 499–514, https://doi.org/10.1007/s13351-020-9161-3.

Zhang, H., 2015: *The Study on Atmospheric Absorption Radiation*. China Meteorological Press, 179 pp. (in Chinese)

Zhang, H., 2016: *BCC_RAD Radiative Transfer Model*. China Meteorological Press, 205 pp. (in Chinese)

Zhang, H., and X. W. Jing, 2016: Advances in studies of cloud overlap and its radiative transfer issues in the climate models. *Acta Meteorologica Sinica*, **74**, 103–113, https://doi.org/10.11676/qxxb2016.009.

Zhang, H., T. Nakajima, G. Y. Shi, T. Suzuki, and R. Imasu, 2003: An optimal approach to overlapping bands with correlated *k* distribution method and its application to radiative calculations. *J. Geophys. Res. Atmos.*, **108**, 4641, https://doi.org/10.1029/2002JD003358.

Zhang, H., G. Y. Shi, T. Nakajima, and T. Suzuki, 2006a: The effects of the choice of the k-interval number on radiative calculations. *Journal of Quantitative Spectroscopy and Radiative Transfer*, **98**, 31–43, https://doi.org/10.1016/j.jqsrt.2005.05.090.

Zhang, H., T. Suzuki, T. Nakajima, G. Y. Shi, X. Y. Zhang, and Y. Liu, 2006b: Effects of band division on radiative calculations. *Optical Engineering*, **45**, 016002, https://doi.org/10.1117/1.2160521.

Zhang, H., and Coauthors, 2012: Simulation of direct radiative forcing of aerosols and their effects on East Asian climate using an interactive AGCM-aerosol coupled system. *Climate Dyn.*, **38**, 1 675–1 693, https://doi.org/10.1007/s00382-011-1131-0.

Zhang, H., J. Peng, X. W. Jing, and J. N. Li, 2013: The features of cloud overlapping in Eastern Asia and their effect on cloud radiative forcing. *Science China Earth Sciences*, **56**, 737–747, https://doi.org/10.1007/s11430-012-4489-x.

Zhang, H., X. Jing, and J. Li, 2014: Application and evaluation of a new radiation code under McICA scheme in BCC_AGCM2.0.1. *Geoscientific Model Development*, **7**, 737–754, https://doi.org/10.5194/gmd-7-737-2014.

Zhang, H., Q. Chen, and B. Xie, 2015: A new parameterization for ice cloud optical properties used in BCC-RAD and its radiative impact. *Journal of Quantitative Spectroscopy and Radiative Transfer*, **150**, 76–86, https://doi.org/10.1016/j.jqsrt.2014.08.024.

Zhang, H., Z. L. Wang, and S. Y. Zhao, 2017: *Atmospheric Aerosols and Their Climate Effects*. China Meteorological Press, 204 pp. (in Chinese)

Zhang, H., X. W. Jing, and J. Peng, 2019: *Cloud Radiation and Climate*. China Meteorological Press, 270 pp. (in Chinese)

Zhao, C. F., and T. J. Garrett, 2015: Effects of Arctic haze on surface cloud radiative forcing, Geophys. *Res. Lett.*, **42**, 557–564, https://doi.org/10.1002/2014GL062015.

Zhao, C. F., and Coauthors, 2020: Aerosol characteristics and impacts on weather and climate over the Tibetan Plateau. *National Science Review*, **7**(3), 492–495, https://doi.org/10.1093/nsr/nwz184.